

Plug-and-Play Nanorization of Coarse Black Phosphorus for Targeted Chemo-photoimmunotherapy of Colorectal Cancer

Wenquan Ou,[†] Jeong Hoon Byeon,^{*,‡} Raj Kumar Thapa,[†] Sae Kwang Ku,[§] Chul Soon Yong,^{*,†} and Jong Oh Kim^{*,†}

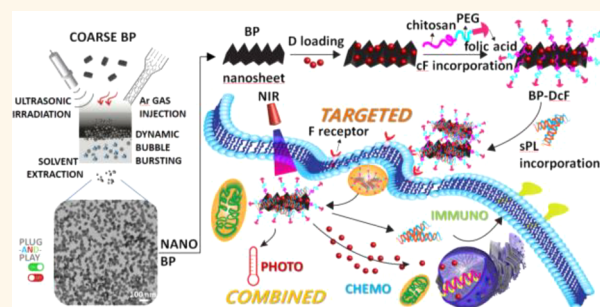
[†]College of Pharmacy and [‡]School of Mechanical Engineering, Yeungnam University, Gyeongsan 38541, Republic of Korea

[§]College of Korean Medicine, Daegu Haany University, Gyeongsan 38610, Republic of Korea

Supporting Information

ABSTRACT: Because of their extraordinary physical properties and biocompatibility, black phosphorus (BP) nanosheets (NSs) have been intensively employed in chemo-phototherapies, such as plasmonic inorganic nanoparticles or graphene NSs, over the past few years. However, most biomedical studies using BP NSs are only concerned with the optical property of BP NSs to repeatedly demonstrate chemo-phototherapeutic efficacies, although BP NSs have different properties from inorganic nanoparticles or graphene NSs, such as corrugated crystal structure, hydrophilicity, and biodegradability. Moreover, it is still a challenging issue to efficiently fabricate uniform BP NSs for clinical translation because of the top-down nature of fabrication, despite the easy preparation of coarse BP flakes. It is thus essential to explore their most suitable bioapplications as well as suggest an easy-to-access strategy to produce uniform BP NSs for realization as advanced therapeutic materials. To rationalize these issues, this report introduces a plug-and-play nanorization, ultrasonic bubble bursting, of coarse BP flakes for continuous BP NS production, and the resulting uniform NSs (~40 nm lateral dimension, ~0.15 polydispersity index) were used as base materials to load drug (doxorubicin), targeting agent (chitosan–polyethylene glycol), and cancer growth inhibitor (programmed death ligand 1 and small interfering RNA) for achieving efficacious chemo-photoimmunotherapy of colorectal cancer.

KEYWORDS: black phosphorus, nanosheets, plug-and-play nanorization, ultrasonic bubble bursting, chemo-photoimmunotherapy



In advanced therapeutics based on nanotechnology, the intrinsic physical properties of inorganic nanoparticles (INPs) have been intensively employed over the last two decades. Specifically, surfaces of noble metal, magnetic, and luminescent NPs, including rare earth elements, have been engineered to utilize their specific optical, magnetic, electrical, or textural properties with biocompatibility for use in a wide range of nanomedicines.¹ Although many feasible surface modification or coordination approaches have been developed to demonstrate efficacious drug delivery, chemo-phototherapies, and targeted combination anticancer therapies, challenges remain regarding cytotoxicity, agglutination, instability, and undegradability of INPs in the human body for biomedical advancements and successful clinical translation.^{2,3} In other words, the components of most INPs are not essential elements of the body; thus, the adoption of INPs in biomedical applications may be associated with toxicity due to immune responses.

The limitations of INPs diverted some attention for nanomedicine research into 2D materials, such as graphene, transition metal dichalcogenides (TMDs), and black phosphorus (BP) because of physical properties comparable with those of INPs.⁴ Although graphene and its derivatives are the longest employed base materials among those for nanomedicines because of their higher biosafety and abundance, there are also questions regarding their clinical realization due to toxicities, harsh preparation, and high production costs, including the absence of a band gap (inducing weak photothermal conversion).^{5,6} In this regard, BP nanoplateforms have been substitutingly used chemo-phototherapies of cancer due to a wide and tunable near-infrared (NIR) response range, biosafety, biodegradability, and ease of preparation.^{6,7} The *in vivo* degradation of BP nanoplateforms into nontoxic phosphate

Received: June 19, 2018

Accepted: September 17, 2018

Published: September 17, 2018

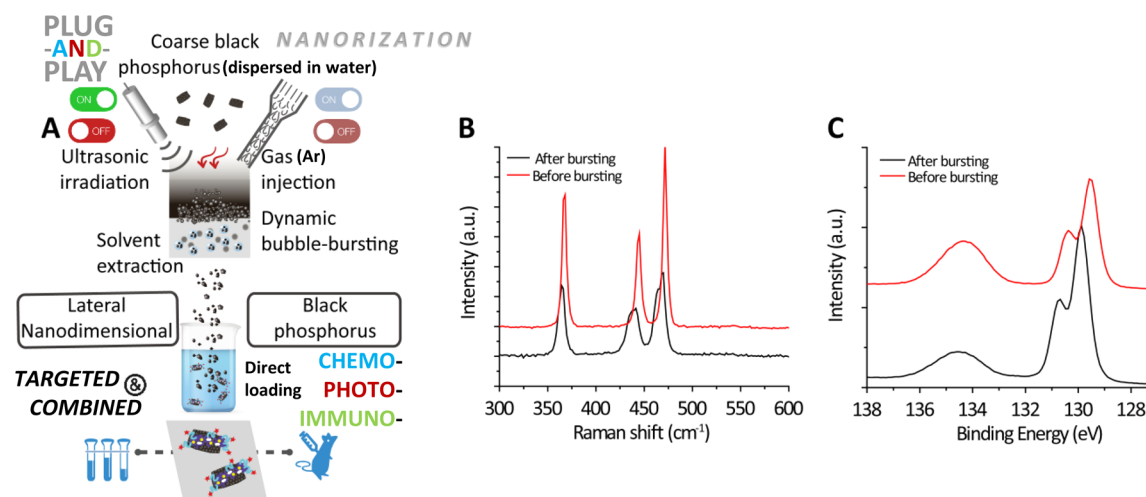


Figure 1. Schematic of the plug-and-play nanorization system to produce BP NSs from coarse BP flakes. (A) Outlines of ultrasonic bubble bursting and combination (chemo-photoimmuno) therapy. Coarse BP flakes were dispersed (0.5 mg/mL) in water (molecular biology grade), and the dispersion was continuously supplied into a probe sonication reactor (60 mL, 150 W) with Ar gas (60 mL/min). Ultrasonically pulverized BP-containing droplets were floated with gas flow *via* bubble bursting at the free surface of dispersion, and the BPs were collected on a substrate to be incorporated with DcF and sPL for use in chemo-photoimmunotherapy. (B,C) Raman and XPS spectra of coarse and nanorized BPs. The spectra of nanorized BPs were compared with the coarse BP flakes to confirm that the nanorized BPs maintained their basic properties after the process.

or phosphonate in aqueous media preferentially confers a safer-by-design concept in the biomedical field.^{8,9} The *in vivo* degradation of BP was specifically validated in chemo-phototherapies more recently.¹⁰ Furthermore, BP nanoplateforms exhibited high drug loading capacity because of corrugated crystalline and textural properties.¹¹ However, BP nanoplateforms have mostly been used for chemo-photo-therapeutic applications to reconfirm the optical properties of the nanoplateforms, similar to that in studies previously attempted with INPs or graphene;⁵ moreover, the chemo-phototherapies may not efficiently remove tumors (*i.e.*, inducing tumor recurrence or metastasis) and be safe to normal tissues.¹² This implies that further development in pursuit of the optimal biomedical applications of NSs is required for clinical realization.^{5,13,14}

Combination cancer therapies have also been recently considered to simultaneously restrict solid tumors, including disseminated and metastatic tumors, because NIR irradiation is inaccessible for disseminated and metastatic tumors to activate phototherapeutic effects.¹⁵ Immunotherapy has recently been introduced in chemo-phototherapies as an emerging combination therapy to activate the host immune system to overcome the limitations of chemo-phototherapies.^{16–18} Complementary immunotherapeutic effects induced synergistic and prolonged anticancer responses to eliminate various types of tumors and their recurrence by applying multifunctional nanoplateforms containing phototransducing and immune-system-stimulating agents.¹⁹ Cancer immunotherapies, in particular, cytotoxic T-lymphocyte (CTL)-associated protein 4 and programmed death 1 (P)/programmed death ligand 1 (PL), have been approved by the U.S. Food and Drug Administration for durable cancer treatments, which act *via* the direct inhibition of cytokine production, attenuation of the cytotoxicity of CD8⁺ T cells (critical for tumor clearance), and T cell lysis-mediated tumor restriction;^{20–22} thus, CTL-associated protein 4 and P/PL blockades modulated the immunosuppressive responses within tumors to improve cancer treatments. These blockades have therefore been

incorporated with hyperthermia (*e.g.*, photo, magneto, or radio) platforms to facilitate strong combination antitumor therapies for minimizing tumor recurrence or metastasis.^{20,23}

In the present study, nanoscale BP was employed to achieve a combinatorial nanoplateform with immunofunction, in consideration of the biomolecule-adsorptive nature of BP.²⁴ Wrinkled BP nanosheets (NSs) with uniform size distribution were prepared *via* plug-and-play nanorization of coarse BP flakes (Figure S1). A plug-and-play system developed herein comprises digitizable ultrasonic bubble bursting, constant coarse BP supply, and unipolar charger (avoiding agglomeration between nanorized BP *via* electrostatic repulsion) devices connected in series in a single-pass argon (Ar) stream to yield lateral nanodimensional BP NSs. The surfaces of NSs (*i.e.*, base phototransducing agent) were first incorporated with doxorubicin (D; for chemotherapy), chitosan–polyethylene glycol (c; for electrostatic loading effect), and folic acid (F; for targetability) to form a chemo-phototherapeutic subplatform (BP-DcF), and this was eventually encapsulated with small interfering RNA (s) and PL (*i.e.*, to block P/PL interaction) to realize BP-DcF@sPL nanoplateforms. Co-adding s with PL for the encapsulation was motivated by the potent gene-silencing activity and high target specificity for cancer immunotherapy,^{25,26} including RNA interference to achieve genetic intervention of the P/PL pathway.²⁷ Furthermore, in a recent paper, it was introduced that uniform BP NPs can be successfully employed as s delivery nanosystems for cancer therapy.²⁸ Combination strategies of BP-DcF@sPL nanoplateforms on colorectal cancer were therefore assessed in the absence and presence of NIR irradiation [for stimulating burst D release and local hyperthermia with reactive oxygen species (ROS) generation] and compared with BP-DcF and BP-DcF + aPL [only PL antibody (aPL) incorporated without s for comparison between BP-DcF@sPL and BP-DcF + aPL in silencing effect], including individual D and NIR configurations (Figure 1A) to confirm the improvement in cancer therapeutic efficacy.

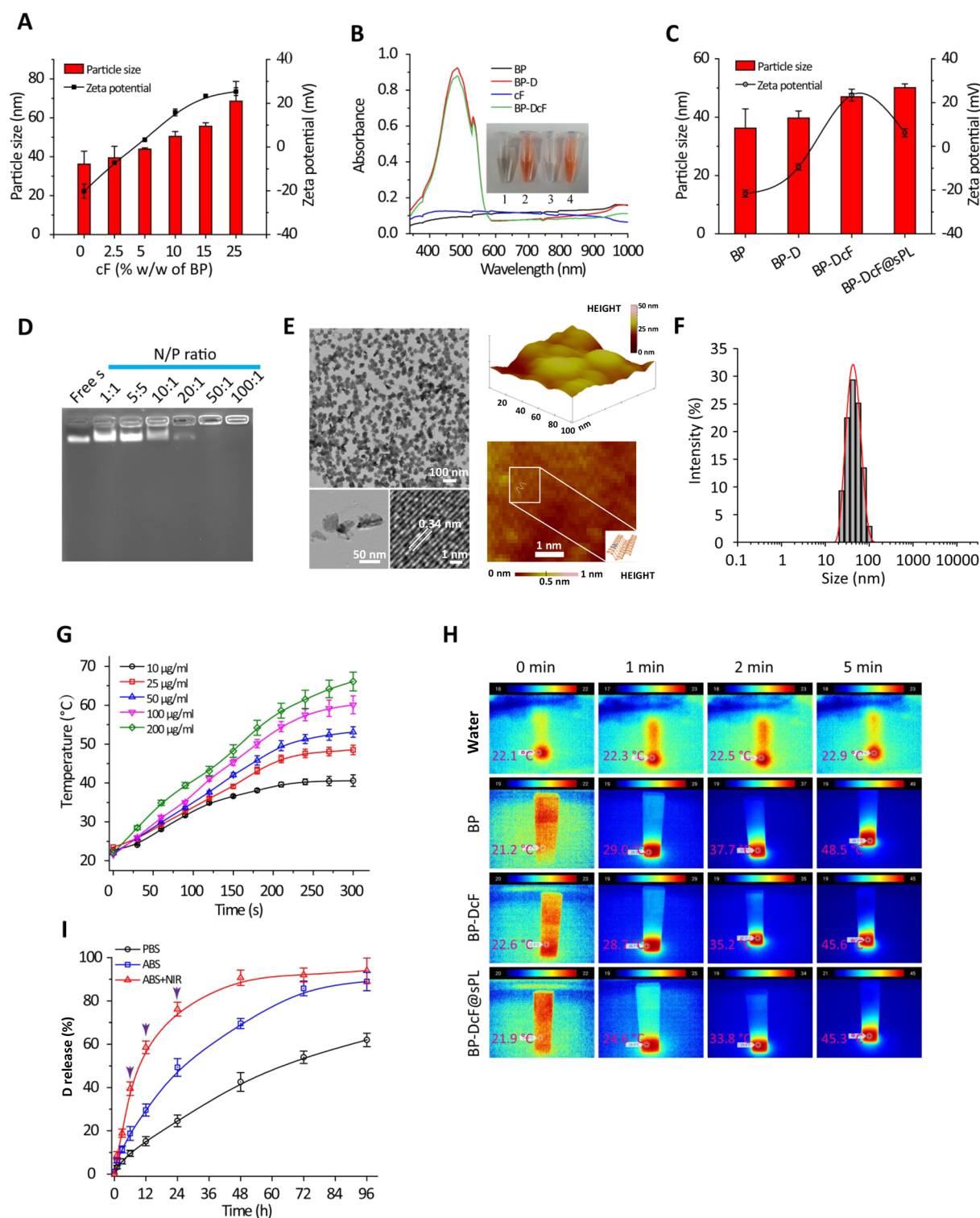


Figure 2. Physicochemical characterizations of nanorized BPs. (A) Changes in particle size and ζ -potential of BP by increasing the cF content ($N = 6$). (B) UV-vis spectra of BP, BP-D, and BP-DcF dispersions ($N = 6$). D and DcF loadings exhibit intensive absorbance around 480 nm, indicating D loading on BP. Inset shows digital images of dispersions, further supporting the D loading. (C) Changes in hydrodynamic size and ζ -potential of BP upon D, DcF, and DcF@sPL loading ($N = 6$). (D) Gel retardation assays to determine an appropriate N/P ratio for sPL loading onto BP-DcF. Low- and high-magnification TEM images with AFM and STM profiles (E) and DLS size distribution (F) of BP-DcF@sPL. (G) Concentration-dependent temperature elevations of BP for 5 min NIR (808 nm, 1.5 W/cm²) irradiation ($N = 6$). (H) Photothermal contours of water, BP, BP-DcF, and BP-DcF@sPL for 5 min NIR irradiation at a fixed concentration (25 $\mu\text{g/mL}$) of BP. (I) *In vitro* D release from BP-DcF@sPL under different conditions (in PBS, in ABS, and in ABS with NIR). Black arrows for “in ABS with NIR” indicate the time points of NIR irradiation (for 5 min, $N = 6$).

We attempted to fabricate BP-DcF@sPL nanoplateforms approximately 50 nm in lateral dimension from uniform base BP NSs [~ 40 nm, ~ 0.15 polydispersity index (PDI)] because the biodistributions of administered NPs are size-specific (<5 nm, cleared by kidney; 50–100 nm, end up in liver and kidney; >2000 nm, accumulate in spleen)²⁹ to efficiently utilize the enhanced permeability retention (EPR) effect; moreover, the smaller size range of 20–200 nm (*i.e.*, effective size range of nanomedicine) may be better for immunotherapy than a larger size.^{18,30} In particular, a previous study reported that BP NSs with larger sizes (several hundred nanometers) exhibited cytotoxicities greater than those of smaller ones (several tens of nanometers,³¹ implying that it is still challenging to provide a suitable supply system of fully lateral nanodimensional base BP to achieve suitable platforms with biosafety for the purpose of obtaining the most efficacious therapeutics. Although BP NSs can be easily prepared by conventional exfoliation methods from coarse BP flakes due to weak interlayer van der Waals interactions,¹³ the exfoliations cannot satisfactorily produce uniform NSs with a lateral nanodimension due to the top-down nature of the preparation.^{32,33} The reagents for exfoliation are also mostly toxic to humans and the environment;³⁴ thus, innovative nanorization of coarse BP flakes is preferentially required to produce uniform BP NSs with minimal biological and environmental hazards. In the present study, plug-and-play nanorization of coarse BP flakes to form uniform BP NSs with a clean surface (for biomedical use) was specifically developed based on bubble bursting³⁵ at the free surface of BP-flake-dispersed water (molecular biology grade) under constant probe sonication and Ar gas supply. This operation enabled continuous size-specific ($d \sim R^{3/8} h^{5/8}$, where d is the mean droplet diameter from bubble bursting, and R and h are the radius and cap thickness of bursting bubbles, respectively) droplet flotation at the free surface through bursting of ultrasonically collapsed bubbles containing pulverized BP and Ar gas. The imbalance between gravity and buoyancy and unipolar charging of the droplets made the size distribution uniform, resulting in the preparation of uniform nanoscale base BP [inset (size distribution measured during the nanorization using scanning mobility particle sizer, SMPS) of Figure S1], maintaining the original surface properties of coarse BP [from comparison in Raman and X-ray photoelectron spectroscopy (XPS); Figure 1B,C] as phototransducing nanovehicles for chemo-photoimmunotherapy.

RESULTS AND DISCUSSION

To confirm cF loading on BP, changes in hydrodynamic particle size and ζ -potential upon cF loading with different concentrations were analyzed, as shown in Figures 2A and S2A. The size and potential were proportional to the cF loading content (wt %); in particular, the negative potential of BP was nearly neutralized at 2.5% cF, and the results exhibited increasing positive potentials by a further increase in cF content (5–25%), implying that cF loading can simultaneously modulate the size and surface charge of BP. Considering the loading of negatively charged s on BP, 10% cF was chosen to secure high positive potential (~ 16 mV) for electrostatic attraction. D loading with different ratios to BP (BP/D) was also performed to evaluate the D loading capacity of BP. The measurements of UV–vis spectra indicated a spectral change of BP upon D loading (Figure S2B), and the color change from gray to red demonstrated the D loading on BP (Figure S2C). There were no significant increases in band intensity for the D

region when the BP/D ratio was greater than 1:1.5, which was consistent with the loading capacity profile (Figure S2D). The UV–vis spectrum of BP-DcF was compared with that of BP-D (Figure 2B) and exhibited comparable loading capacity (Figure S2E). The particle size and surface charge upon DcF loading on BP reached approximately 48 nm and 23 mV, respectively (Figure 2C); thus, BP-DcF was capable of loading the negatively charged s due to its cationic nature. This was verified by a gel retardation assay at different nitrogen to phosphate (N/P) ratios, and s was strongly attached to BP-DcF at ratios greater than 20:1 (Figure 2D). The BP-DcF still exhibited a positive surface charge (6.2 mV; modest positive potential for cellular interaction and s transfection with minimal cation-mediated cytotoxicity)³⁶ even upon sPL loading; furthermore, the loading did not exhibit a significant size increase (<50 nm) and loading capacity decrease (93%; Figure S2E). The transmission electron microscopy (TEM) image of BP-DcF@sPL (Figure 2E) exhibits anisotropic structures with a lateral dimension of 46.0 ± 3.2 nm (200 particles analyzed), which matched the hydrodynamic size distribution measured by the dynamic light scattering (DLS) system (50.1 ± 1.3 nm; Figure 2F). The slight difference in size between the observations might have been due to the different states of the specimens (dried powder *vs* dispersion); the swelling of the nanoplateform in the DLS measurement might have caused the size difference. Nevertheless, the size of the nanoplateform was within the effective range for the EPR effect, even in a swollen state. The high-magnification TEM images of BP from plug-and-play nanorization before loading DcF@sPL (the bottom panels of Figure 2E) showed wrinkles (*i.e.*, transformation of NS) within the anisotropic shape and the intrinsic crystal feature of BP [0.34 nm d -spacing, (021) plane], implying that the nanorization was workable to produce BP NSs without microstructural deformation. The shape of BP was further examined using atomic force microscopy (AFM; right upper image of Figure 2E), and the resulting topograph supported the wrinkled (not planar) structure from ultrasonic bubble bursting.³⁷ The microstructure of BP observed using scanning tunneling microscopy (STM; right lower image of Figure 2E) matched a puckered honeycomb lattice structure.³⁸ The DcF@sPL incorporation with BP NSs was further confirmed by comparing spectra between BP-DcF@sPL and individual components in Fourier transform infrared (FTIR) and X-ray diffraction (XRD) analyses (Figure S3). The merged spectral characteristics between the components suggest that the NS texture from nanorization was appropriate to tightly load DcF@sPL on the surface. The loading of DcF on the surfaces of BP NSs was further examined using energy-dispersive X-ray spectroscopy (EDS; Figure S4), proving the coexistence of three more elements (*i.e.*, C, N, and O from the surface loading of DcF) with BP (represented as P). Maintenance of the intrinsic property after nanorization was also identified by recording both time- and dose-dependent temperature elevations of the NSs using a thermal camera under NIR irradiation (808 nm, 1.5 W/cm²) for 5 min. The temperature of NSs reached 70 °C upon irradiation at 200 μ g/mL (Figure 2G), and stable elevations were also proven for BP-DcF (22.6–45.6 °C) and BP-DcF@sPL (21.9–45.3 °C) nanoplateforms even after six cycles of irradiation (Figure 2H). The cumulative D release for 96 h of measurement in different media [acetate-buffered saline (ABS) pH 5.0 and phosphate-buffered saline (PBS) pH 7.4] exhibited site-selective release [reached 88.4% at ABS

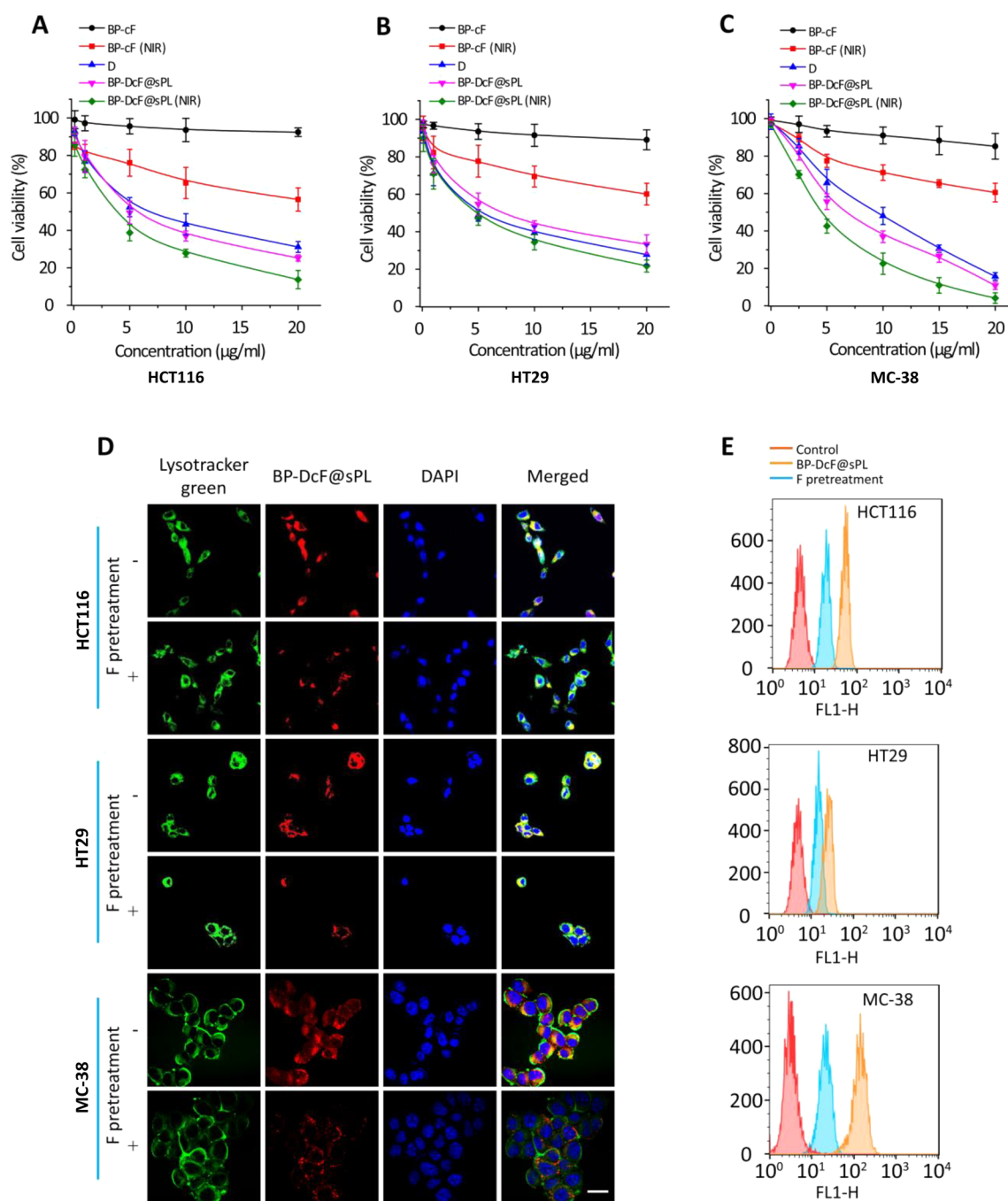


Figure 3. Cytotoxicity and uptake of BP-DcF@sPL in different cell lines. (A–C) Cytotoxicity profiles of BP-DcF@sPL with and without NIR irradiation (808 nm, 3.0 W/cm², 5 min) in HCT116, HT29, and MC-38 cells. The results were compared with D and BP-cF (with and without NIR irradiation, $N = 6$). (D) Confocal images of the cells incubated with BP-DcF@sPL with and without F pretreatment. Lysotracker green and DAPI were also used for comparison purposes. Scale bar, 20 μm . (E) FACS analyses to evaluate the cellular uptake of BP-DcF@sPL with and without F pretreatment.

(simulated tumor microenvironment), 2 times greater than at PBS]. During the study period, the D release was further facilitated (reached 91.0% within 48 h) by NIR irradiation (for 5 min at time points at 8, 12, and 24 h) due to photothermal effect-triggered release (Figure 2I). The stability of loaded D on BP-DcF@sPL was investigated by incubation of BP-DcF@sPL in the mouse serum for 24 h. No significant decreases (*i.e.*, nonselective D release) were detected during the period, demonstrating the validity of electrostatic conjugation

between BP and D to avoid undesirable release of D during circulation (Figure S5).

Cytotoxic effects of BP-DcF@sPL nanoplateforms (0–20 $\mu\text{g/ml}$) to HCT116 (Figure 3A), HT29 (Figure 3B), and MC-38 (Figure 3C) cells were assessed by 3-(4,5-dimethylthiazol-2-yl)-5-(3-carboxymethoxyphenyl)-2-(4-sulfophenyl)-2H-tetrazolium (MTS) assay in the absence and presence of NIR irradiation and compared with BP-cF (with and without NIR) and free D. The results from BP-cF (without NIR) and free D demonstrated that BP-cF before D loading is biocompatible

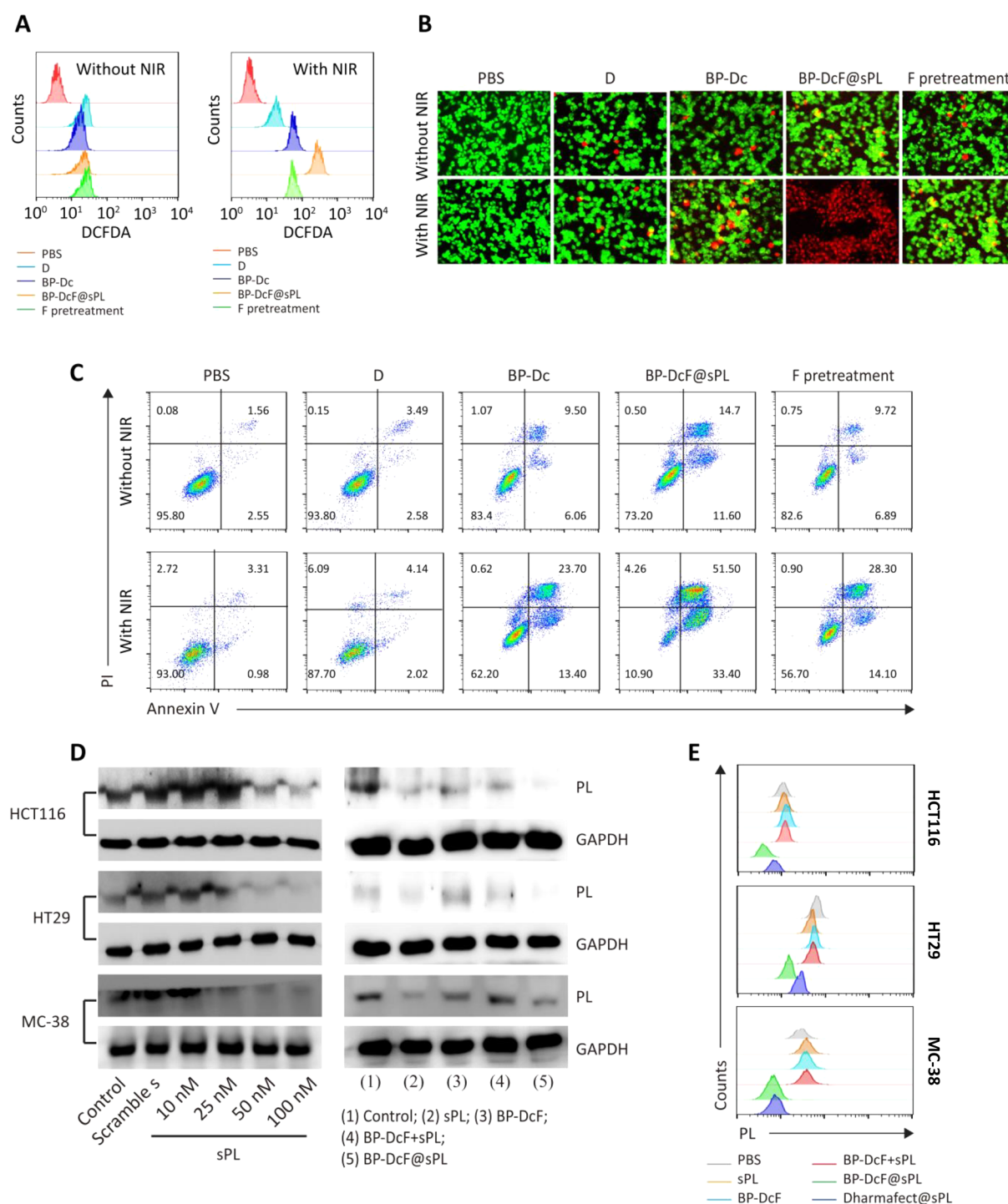


Figure 4. Anticancer studies based on ROS generation, live/dead cell staining, apoptosis, Western blot, and PL expression assays. (A–C) ROS generation, live/dead, and apoptosis assays of MC-38 cells after incubation with BP-DcF@sPL with and without F treatment, including PBS, D, and BP-Dc for comparison purposes in the absence and presence of NIR irradiation (808 nm, 1.5 W/cm², 5 min, *N* = 3). (D) Analyses of PL gene silencing in HCT116, HT29, and MC-38 cells after treatment with BP-DcF@sPL at different sPL concentrations and configurations (including control, sPL, BP-DcF, and BP-DcF+sPL at an s concentration of 50 nM, *N* = 3). (E) PL expression analyses using FACS in HCT116, HT29, and MC-38 cells from treatments with PBS, sPL, BP-DcF, BP-DcF+sPL, BP-DcF@sPL, and Dharmafect@sPL.

and warrants further bioassays to assess therapeutic efficacies. The increased cytotoxicities of BP-cF upon NIR irradiation support the intrinsic phototherapeutic efficacies of BP NSs. Interestingly, the cytotoxicity of BP-DcF@sPL nanoplatform (without NIR) was greater than that of free D to all cell lines, although BP-cF exhibited biocompatibility. This may be explained by the folate-mediated cellular uptake being greater

than that for free D, where the targeted D delivery into the cells induced greater cytotoxicity (more than 50% cell death at 10 μ g/mL) than for free D. Upon NIR irradiation to BP-DcF@sPL-treated cells, over 60% cell death was achieved even at 5 μ g/mL, probably due to the enhancement of photothermal-effect-triggered D release and subsequent ROS generation. Intracellular D fluorescence intensities (evidenced

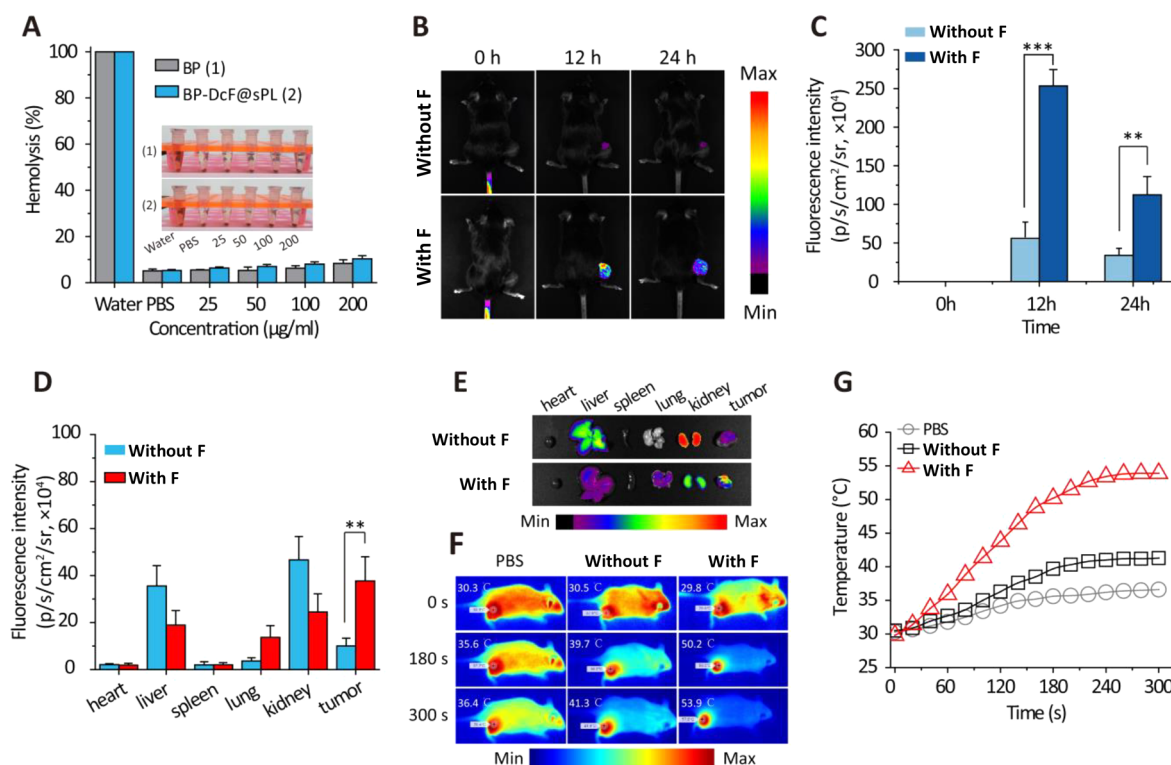


Figure 5. Hemolysis of BP-DcF@sPL, including *in vivo* biodistribution and photothermal activity. (A) Percentage hemolysis of RBCs at different concentrations of BP and BP-DcF@sPL. Inset shows relevant digital images from the tests ($N = 3$). (B,C) *In vivo* biodistributions and corresponding fluorescence intensities of Cy5.5-labeled BP-Dc@s (i.e., without F) and BP-DcF@s (i.e., with F) at 0, 12, and 24 h postinjection ($N = 6$). (D,E) Fluorescence intensities and corresponding *ex vivo* biodistributions of Cy5.5-labeled BP-Dc@s (i.e., without F) and BP-DcF@s (i.e., with F) in heart, liver, spleen, lung, kidney, and tumor 24 h postinjection ($N = 6$). (F,G) Photothermal contours and corresponding temperature elevation profiles in the tumor region of MC-38 tumor-bearing mice treated with Cy5.5-labeled BP-Dc@s (i.e., without F) and BP-DcF@s (i.e., with F), including PBS for comparison purposes under NIR irradiation (808 nm, 1.5 W/cm², 5 min).

by colocalization with lysosomes) from the BP-DcF@sPL uptake for untreated and F-pretreated cells (HCT116, HT29, and MC-38) were visualized using confocal laser scanning microscopy (CLSM) to confirm folate-mediated enhanced D delivery (Figure 3D). The attenuation of D fluorescence for F-pretreated cells was caused by the receptor saturation upon F pretreatment, evidencing the folate-mediated D targeting. The Western blot results (Figure S6) exhibited a folate receptor expression in the three cell lines, which are consistent with a previous report.³⁹ The highest folate receptor expression in MC-38 cells supported the greater uptake of MC-38 cells compared with HCT116 and HT29 cells. These results were quantitatively confirmed by flow cytometry (Figure 3E), implying that the inclusion of F confers targetability to a nanoplateform for better internalization. The escape of s from endosome was also observed using CLSM, displaying dissociation of s (green color) from lysosome (red color) in HCT116, HT29, and MC-38 cells (Figure S7).

The effect of NIR irradiation on ROS generation was evaluated using dichlorodihydrofluorescein diacetate (DCFDA) assay for MC-38 cells (Figure 4A). There were no significant differences in ROS level between BP-Dc and BP-DcF@sPL platforms (with and without F pretreatment) in the absence of NIR irradiation. ROS levels of the platforms (resembling each other) were lower than that from free D, whereas the levels significantly increased upon NIR irradiation. In particular, the irradiation significantly promoted the ROS generation of the BP-DcF@sPL platform, which was due to folate-mediated enhanced uptake for synergistic apoptotic

effects from chemo (D)- and photo (BP NS)-therapeutics, proven by comparison with the F-pretreated configuration (i.e., inducing receptor saturation to block platform internalization into the cells, thus exhibiting ROS generation comparable to that of the F-absent platform, BP-Dc). This synergistic apoptosis of BP-DcF@sPL with NIR was further examined by comparative live (green fluorescence)/dead (red fluorescence) assays (Figure 4B). The F-absent (i.e., BP-Dc) and F-pretreated (i.e., receptor-saturated) configurations did not significantly induce apoptotic cell death due to their low internalization and activation of D efflux receptors.⁴⁰ The fraction of apoptotic MC-38 cells was quantified by flow cytometry using an Annexin V/propidium iodide (PI) double staining kit in the absence and presence of NIR irradiation (Figures 4C and S8). The early (6.06%) and late (9.50%) apoptotic percentages from BP-Dc treatment without NIR increased to 11.60 and 14.70% by adding F and sPL, respectively, and these were significantly enhanced further with NIR (33.40 and 51.50%, respectively), suggesting that NIR irradiation significantly promoted apoptosis. The F pretreatment for receptor saturation decreased apoptosis (14.10 and 28.30%) even at NIR irradiation, which implies that the additions of F and NIR enhance the cellular internalization of nanoplateform and ROS generation to increase cytotoxicity against cancer cells. In a Western blot assay to validate the gene-silencing effect of the BP-DcF@sPL nanoplateform (Figure 4D), HCT116, HT29, and MC-38 cells were incubated with 20 ng/mL IFN- γ with different sPL concentrations on BP-DcF as the production of IFN- γ by

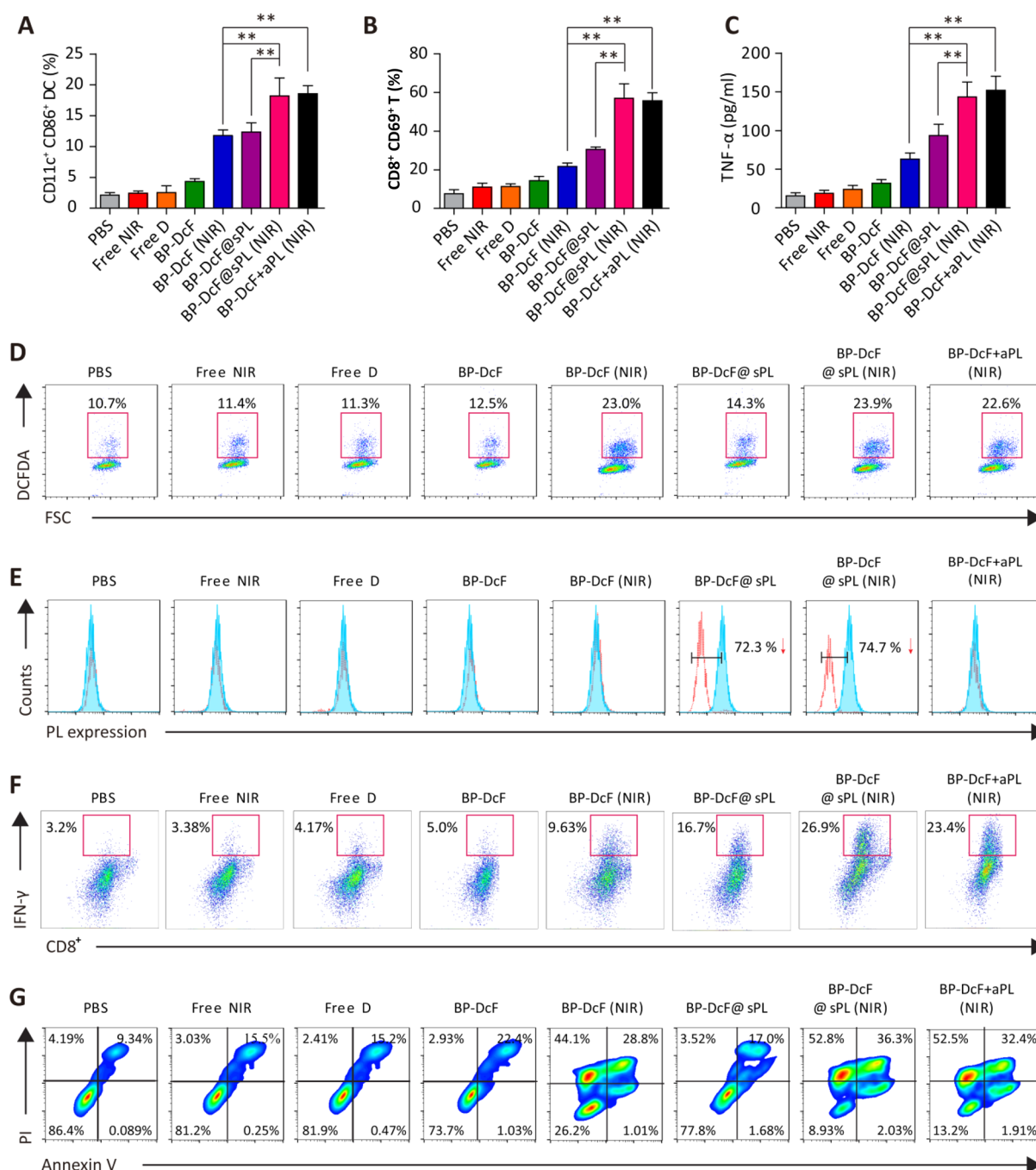


Figure 6. Antitumor T cell and apoptotic responses in the tumor microenvironment of MC-38 tumor-bearing mice after treatments with BP-DcF and BP-DcF@sPL in the absence and presence of NIR irradiation, including individual PBS, NIR, and D with BP-DcF+aPL (in the presence of NIR) for comparison purposes ($N = 6$ for each group, $**p < 0.01$, $***p < 0.001$). (A,B) FACS analysis of the percentages of matured DCs (characterized by CD11c⁺ CD86⁺) and activated CD8⁺ T cells (characterized by CD8⁺ CD69⁺). (C) ELISA analyses to determine TNF-α expression levels. (D–G) DCFDA-specific ROS generation (forward scatter, FSC), PL expression, IFN-γ-specific CD8⁺ T cells, and Annexin V/PI staining-specific apoptotic tumor cell levels.

tumor-infiltrating CTLs could stimulate PL expression on tumors, and the existence of IFN-γ in the culture medium was proven to promote PL expression in colon cancer or melanoma.^{41,42} MC-38 cells rapidly expressed high PL signals upon IFN-γ stimulation. HCT116 cells also expressed intense signals but showed slower response than MC-38 cells, requiring 24 h post-IFN-γ incubation. Even though HT29 cells exhibited PL expression weaker than that of HCT116 and MC-38 cells, the stronger signals can be seen in the case of IFN-γ-free condition (Figure S9). The assay demonstrated that

PL expression was downregulated in a manner dependent on the dose of sPL; in particular, BP-DcF@sPL exhibited significantly reduced PL expression (*i.e.*, silencing effect) compared with BP-DcF and BP-DcF+sPL (by sPL mixing). The results (Figure 4E) also revealed PL expression for BP-DcF@sPL significantly lower than that with other configurations, and the level was comparable to that with commercial Dharmafect transfection agent (*i.e.*, Dharmafect@sPL), proving the feasibility of the gene-silencing effect of BP-DcF@sPL. To measure the simulated competitive cellular uptake between

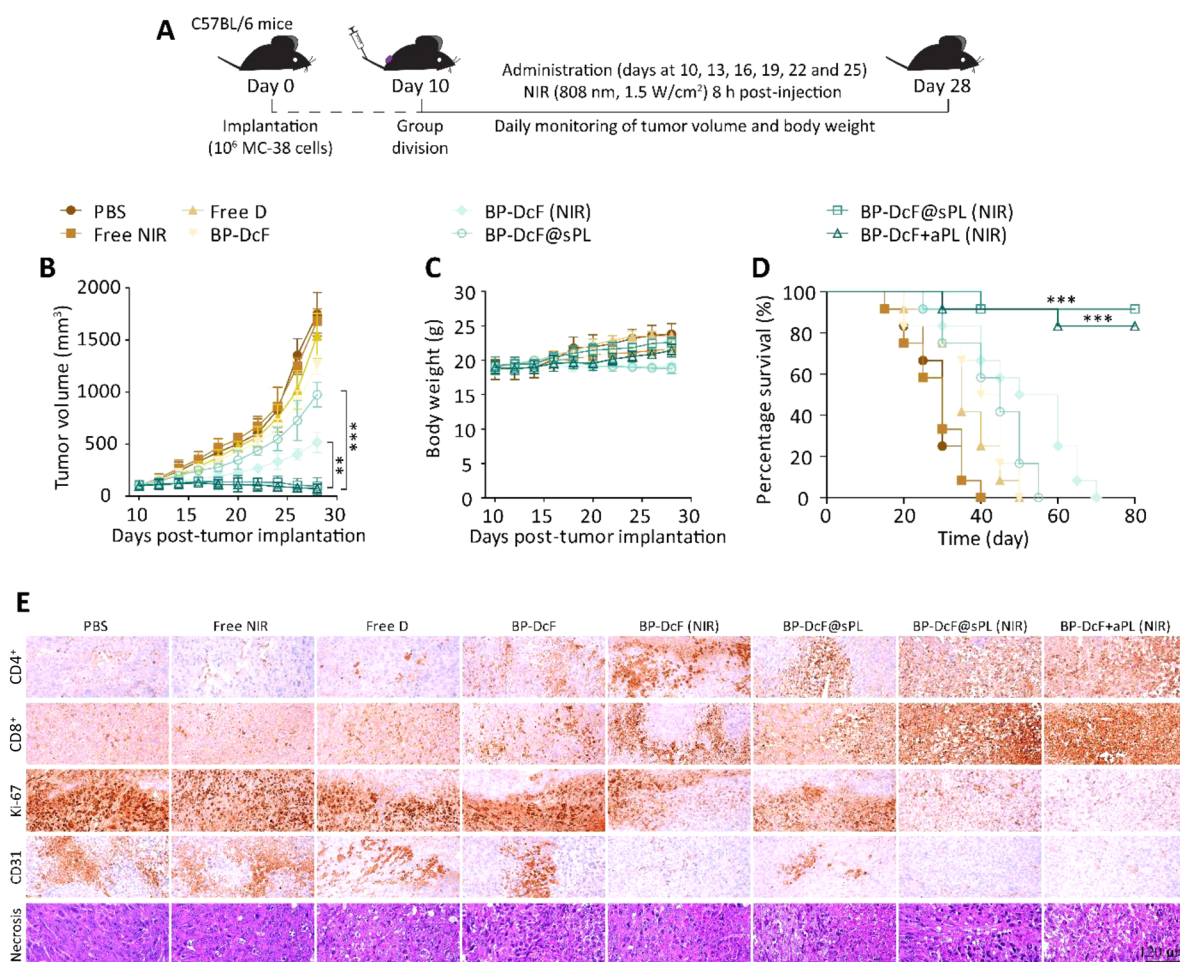


Figure 7. Potent therapeutic efficacies of BP-DcF and BP-DcF@sPL in the absence and presence of NIR irradiation, including individual PBS, NIR, and D with BP-DcF+aPL (in the presence of NIR) for comparison purposes against a MC-38 tumor *via* monitoring of tumor volume, body weight, and survival rate ($N = 6$ for each group, $**p < 0.01$, $***p < 0.001$), as well as performing immuno-histochemical and histopathological staining. (A) Schematic of the therapy regimen. The sample injections were performed and continued at days 10, 13, 16, 19, 22, and 25 when the tumor size reached 100 mm^3 . The NIR irradiation (808 nm , 1.5 W/cm^2 , 5 min) was applied at 8 h after each injection. (B,C) Average tumor volumes and body weights of the treated mice. (D) Percentages of surviving mice with different treatments. (E) Representative optical microscope images of tumor sections showing H&E staining and levels of CD4⁺, CD8⁺, Ki-67, CD31, and necrosis after the treatments. Scale bar, $120 \mu\text{m}$.

tumor-infiltrating lymphocytes (TILs) in the tumor micro-environment, MC-38 cells were also cocultured with CD8⁺ T, dendritic, or RAW264.7 (macrophage) cells using Transwells (Figure S10A). The results (Figure S10B,C) indicated that uptake of BP-DcF@s significantly greater than that of BP-Dc@s (no F) was only found for MC-38 cells, whereas there was no significant difference in the uptake between the configurations in CD8⁺ T, dendritic, and RAW264.7 cells (within smaller uptakes than for BP-DcF@s), which further supported the tumor-selective internalization.

From hemolysis assays (Figure 5A), it could be concluded that there were no significant hemolytic effects from both BP NS and BP-DcF@sPL even at $200 \mu\text{g/mL}$ compared with PBS negative control group. The negative surface charge of BP NSs may limit the coagulation between the BP and red blood cells (RBCs), resulting in less release of hemoglobin, whereas c in BP-DcF@sPL may protect the interaction with RBCs. These results indicated again the biocompatibility and systemic circulation of BP NS and BP-DcF@sPL. The tumor-targeting property of BP-Dc@s was examined after the intravenous injection of BP-Dc@s with and without F upon cyanine 5.5

(Cy5.5) conjugation into MC-38 tumor-bearing mice (Figure 5B). The inclusion of F induced a fluorescent signal more than two times higher at the tumor site at 12 and 24 h postinjection due to folate-mediated tumor cell targeting (Figure 5C). The difference in fluorescence intensities between the tumors and the major organs further supported the tumor-selective accumulation of BP-Dc@s due to the inclusion of F in them (Figure 5D,E). The distribution of D after 24 h upon intravenous injection of BP-DcF@sPL exhibited a greater tumor accumulation compared with the injection of free D, supporting stronger antitumor effect (Figure S11). The tumor-selective temperature increases were then measured by a thermal camera during NIR irradiation (808 nm , 1.5 W/cm^2 , 5 min) at 6 h postinjection (Figure 5F). BP-DcF@s exhibited the highest temperature ($53.9 \text{ }^\circ\text{C}$) from 5 min irradiation, which was significantly higher than that for BP-Dc@s ($41.3 \text{ }^\circ\text{C}$), confirming the targeting effect of F. Interestingly, only 3 min irradiation sufficiently increased the temperature ($50.2 \text{ }^\circ\text{C}$ for BP-DcF@s; Figure 5G), suggesting that BP NSs were effective phototransducing base materials to generate hyperthermia even for *in vivo* models.

To determine immune responses (*i.e.*, TILs in the tumor microenvironment) from NIR irradiation and sPL blockade against tumors, as introduced in previous reports [*e.g.*, maturing dendritic cells (DCs), accumulating CD8⁺ T cells, releasing cytokines, and inflammatory mediators],^{26,43,44} MC-38 tumor-bearing mice were treated with BP-DcF and BP-DcF@sPL in the absence and presence of NIR irradiation (808 nm, 1.5 W/cm², 5 min, 8 h postinjection), including individual PBS, NIR, and D with BP-DcF+aPL (in the presence of NIR) for comparison purposes. BP-DcF@sPL with NIR exhibited a higher proportion of CD11c⁺ CD86⁺ matured DCs (~20%; Figure 6A) than for other configurations (BP-DcF with and without NIR; BP-DcF@sPL without NIR). The results clarified the effectiveness of sPL (BP-DcF *vs* BP-DcF@sPL); nevertheless, the absence of s could also be compensated by NIR irradiation when sPL was substituted with PL (*i.e.*, BP-DcF+aPL; showing similar maturation of DCs). Analogous results were found in CD8⁺ CD69⁺ T cells; in particular, approximately 37% activated T cells were found at BP-DcF@sPL with NIR, which was also comparable with the finding for BP-DcF+aPL with NIR (Figure 6B). This trend was also found for the intratumoral concentration of TNF- α measured by ELISA (Figure 6C) and *in vivo* ROS generation using DCFDA probe (Figures 6D and S12A), proving the efficacious consistency of BP-DcF@sPL with NIR. The *in vivo* gene-silencing effect (*i.e.*, PL downregulation that promotes CD8⁺ T cell infiltration into the tumor microenvironment⁴⁵) of BP-DcF@sPL was higher than those of other configurations, whereas NIR irradiation onto BP-DcF@sPL did not significantly increase the silencing effect, whereas other groups also exhibited levels similar to the control groups (Figure 6E); this implies that gene silencing depends more dominantly on sPL encapsulation. The expression levels of IFN- γ (the vital parameter for activation and infiltration of CTLs^{41,46}) in CD8⁺ T cells from BP-DcF@sPL or BP-DcF+aPL treatment were greater than that for other configurations, even without NIR (Figures 6F and S12B), demonstrating that PL incorporation is a critical parameter for inducing greater infiltration of CD8⁺ T cells in the tumor microenvironment. *In vivo* tumor cell necrosis and apoptosis of the treatments were measured using an Annexin V/PI kit to further confirm the immuno-antitumor effects with NIR and sPL (Figures 6G and S12C). NIR irradiation onto BP-DcF and BP-DcF@sPL, including BP-DcF+aPL, induced significant increases in both necrosis (44.1–52.8% due to hyperthermic direct cell death) and apoptosis (28.8–36.3%); in particular, PL-containing configurations exhibited apoptosis levels higher than those of BP-DcF *via* PL downregulation in cancer cells, inducing enhancement of the immuno-antitumor effect guided by CD8⁺ T cells.

The systemic therapeutic effects of treatments were investigated using MC-38 tumor xenografted in C57BL/6 mouse models (Figure 7A). BP-DcF@sPL (82%) and BP-DcF+aPL (80%) with NIR exhibited significant reductions of tumor growth (Figures 7B and S13) without significant weight losses (Figure 7C) compared with other configurations, including controls (PBS, D, and NIR; exhibited negligible effects on tumor growth). The free D group did not exhibit significant antitumor activities probably due to a poor EPR effect, where insufficient retention of D at the tumor site was provided for inducing antitumor activity.¹¹ Eventually, BP-DcF@sPL (90%) and BP-DcF+aPL (80%) with NIR dramatically promoted the survival rate even after 80 days (Figure 7D), which were much more efficacious than in other

groups even with NIR; this proved the sustained antitumor activity from the developed chemo-photoimmunotherapy. From the histopathological and immunohistochemical analyses of tumor masses (Figure 7E), it could be concluded that mice treated with BP-DcF@sPL and BP-DcF+aPL with NIR displayed significantly greater accumulation of CD4⁺ or CD8⁺ T cells, whereas they induced decreases in the expression level of Ki-67 (represents tumor cell proliferation) or CD31 (represents angiogenesis), proving further the greater tumor necrosis *via* the combination therapy against tumors. The results of the analyses are presented in Table S1. Hematoxylin and eosin (H&E) staining of the major organs (heart, liver, spleen, lung, and kidney) after the treatments indicated no significant damage (Figure S6), reflecting the biosafety of the combination therapy.

The extendability of BP-DcF@sPL with NIR into other colorectal cancers was further verified by adopting HCT116-bearing Balb/c nude mice. The resistance of BP-DcF@sPL and BP-DcF to tumor growth was significantly enhanced by NIR irradiation, exhibiting reductions ~1.5 times greater than those in the absence of NIR (Figures S15 and S16A). There were no significant differences in antitumor effect between the BP-DcF@sPL and BP-DcF treatments due to the lack of functional T cells in the mice. Although variations in the body weight from the treatments could not be found during the period (Figure S16B), BP-DcF@sPL and BP-DcF with NIR promoted the survival rate even after 70 days (Figure S16C). The greater antitumor effects detected in MC-38 tumor xenografted in C57BL/6 mouse (*i.e.*, immunocompetent) models compared with HCT116-bearing Balb/c nude mice (*i.e.*, immunocompromised) further suggest a modulatable efficacy of the developed nanoplatforms that may confer various on-demand immuno-approaches for an optimal regimen for treating cancer.

CD4⁺, CD8⁺, or CD4⁺–CD8⁺ T cell-blocking mice were used to confirm the efficacies of T cells in antitumor therapy. The results show that mice upon intraperitoneal injection (on days 0 and 5) of anti-CD4, -CD8, or -CD4–CD8 at a dose of 10.0 mg/kg per mice could successfully form CD4⁺, CD8⁺, or CD4⁺–CD8⁺ mice (Figure S17). Immunoglobulin G (IgG) injection did not influence the antitumor effect of BP-DcF@sPL with NIR, whereas blocking CD4⁺, CD8⁺, or CD4⁺–CD8⁺ T cells significantly affects the efficacy of BP-DcF@sPL with NIR for inhibiting tumor growth (Figure S18), suggesting the essential role of CD4⁺ and CD8⁺ T cells for the tumor therapy.

CONCLUSION

A plug-and-play nanorization of coarse BP flakes *via* ultrasonic bubble bursting was developed to continuously produce uniform BP NSs (~40 nm lateral dimension, ~0.15 PDI) without the use of wet chemistry and additional size classifications. Simultaneous ultrasonic BP pulverization and bubble bursting under inert gas flow introduced size-selective floating from the force imbalance between gravity and buoyancy, resulting in the continuous supply of uniform BP NSs. The toxic-chemistry-free route could allow direct loading of DcF and sPL on the NSs to fabricate BP-DcF@sPL nanoplatforms without further purification. The resulting NSs exhibited a hyperthermic effect and burst D release upon NIR irradiation due to photothermal activity, and cF loading utilized sPL incorporation due to electrostatic attraction during the nanoplatform fabrication and tumor accumulation *via* F receptor targeting during the bioapplication. The BP-DcF@

sPL configuration not only induced chemo (apoptosis/necrosis)-phototherapeutic (local heat and ROS generation) effects but also interfered with PL pathway-regulated immune tolerance and suppression of CD8⁺ T cells (*i.e.*, inducing cancer cell lysis effect because of IFN- γ and TNF- α). The NIR-induced maturation of DCs further enhanced the lysis effect due to promotion of the infiltration of T cells into the tumor microenvironment, implying that the proposed nanoplateforms with NIR can suitably elicit collective activation of the immune system. These multiple therapeutic effects were thus feasible in both C57BL/6 and Balb/c nude mouse models; in conclusion, the survival period of the treated group was significantly prolonged and lasted. The findings not only provide a feasible nanorization system to supply uniform base BP to be directly incorporated with biofunctional components at the nanoscale but also suggest an efficient combination (targeted chemo-photoimmuno) therapy strategy to improve the efficacies of widely recognized chemo-phototherapies.

METHODS

Plug-and-Play Nanorization of Coarse BP Flakes. Coarse BP flakes from chemical vapor transport reaction⁴⁷ were first dispersed in molecular biology grade water (HyClone, GE Healthcare Life Sciences, USA; to prevent degradation of BP)¹¹ to fill the reservoir (500 mL) and probe sonication reactor (60 mL volume). The nanorization of coarse BP flakes was continuously performed by turning on a probe sonicator (150 W, Sonics & Materials, USA) with flow and collection devices with a plug-and-plug single-pass configuration. Specifically, the dispersion (0.5 mg/mL) in the reservoir was constantly supplied (1 mL/min) using a peristaltic pump (323Du/MC4, Watson-Marlow Bredel Pump, USA) into the sonication reactor under Ar gas injection [60 mL/min using a mass flow controller (Kojima, Japan)]. The dispersed BP flakes were ultrasonically pulverized in the reactor (residence time of the dispersion: 1 h), and burst droplets containing the pulverized BP (*i.e.*, BP NS) were floated at the free surface of the dispersion. Owing to the force imbalance between gravity and buoyancy with ultrasonic bubble collapsing, the droplets with a specific size were floated and flowed along with positively ionized Ar gas [further injected using another mass flow controller right next to the free surface for dilution (10 times) and unipolar diffusion charging of the floated droplets] to suppress agglomeration of the droplets. The droplets were then dried by passing through a diffusion dryer (silica gel packed hollow tube); therefore, BP NSs were electrostatically collected on a polished duralumin rod with a negative electric field (−2 kV/cm). Also, the probe sonication reactor was enclosed with a ring-type Peltier cooler (TE Technology, Inc., USA) to prevent overheating of the reactor during the sonication.

Preparation of BP-DcF@sPL Nanoplateforms. Dried BP NSs (10 mg) from the nanorization were redispersed in deoxygenated water (10 mL) for the incorporation of DcF and sPL. Ten percent cF (w/w of BP) was mixed with D (1.0:5.0 mass ratio of BP/D) and then added into the dispersion in an ice water bath under ultrasonication for 30 min. After being stirred for 3 h to form BP-DcF, 50 nM s was dropped into the solution, incubated overnight under stirring, and purified using a dialysis bag (MW = 3500 kDa). To analyze the loading efficiency and capacity, different D contents as BP/D were applied to the preparations of BP-D, BP-DcF, and BP-DcF@sPL, and D contents were measured using high-performance liquid chromatography (HPLC; CM5000, Hitachi, Japan).

Physicochemical Characterization. *In situ* analyses of size distribution during the nanorization were performed using SMPS (3936; TSI, USA) by direct sampling of BP NS-laden Ar gas flow. Surface structures of dried BP NSs were compared using Raman spectroscopy (XploRA Plus; HORIBA, Japan) and XPS (Axis-HIS; Kratos Analytical, Japan). Light absorption spectra of D- or DcF-loaded BP NSs were measured using UV–vis spectroscopy (U-2800;

PerkinElmer, USA). The hydrodynamic size distribution (*via* DLS) and ζ -potential of BP-cF at different cF contents (0–25%) were analyzed using Zetasizer (Nano-S90; Malvern Instruments, UK). Morphology and microstructure were confirmed using TEM (Tecnai G² F20 S-TWIN; FEI, USA), AFM (NanoscopeIIIa, Digital Instruments, USA), and STM (NanoscopeIIIa ECSTM, Digital Instruments, USA). Gel retardation assay using 3% agarose gel (Invitrogen, USA) containing GelRed nucleic acid stain (Biotium, USA) was used to determine the optimal N/P ratio between BP-DcF and s. To measure photothermal activity, the dispersions with different concentrations (10–200 μ g/mL) were irradiated (808 nm, 1.5 W/cm²) for 5 min, and the temperatures were recorded using a digital thermal camera (Therm-App TH, Israel). Incorporations of DcF and sPL with BP NSs were qualitatively analyzed *via* EDS (INCA 350, Oxford Instruments, UK), FTIR spectroscopy (Nicolet Nexus 670; Thermo Fisher Scientific, USA), and XRD (D/MAX-2500; Rigaku, Japan).

In Vitro D Release. *In vitro* D release from BP-DcF@sPL was assessed by an equilibrium dialysis method using a dialysis bag (MW = 3500 kDa). Briefly, 1.0 mL of BP-DcF@sPL was added into the dialysis bag and incubated in 30 mL of PBS (pH 7.4) or ABS (pH 5.0) at 37 °C and 100 rpm (shaking speed). One milliliter of the released medium was withdrawn at time intervals of 0.0, 1.5, 3.0, 6.0, 12.0, 24.0, and 48.0 h, followed by supplementation with an equal volume of fresh medium. The effect of NIR irradiation (808 nm, 1.5 W/cm², 5 min) on D release in ABS was assessed at time points of 1.5, 3.0, and 6.0 h. Cumulative D release was estimated by measuring D concentrations using HPLC (CM5000, Hitachi, Japan). The loading stability of BP-DcF@sPL in the serum was examined by measuring the D contents at 0, 4, 8, 12, and 24 h.

Cell Culture. MC-38 cells were obtained from Kerfast (Boston, MA, USA), and HCT116 and HT29 cells were purchased from American Type Culture Collection. The cells were cultured in Dulbecco's modified Eagle's medium containing 10% fetal bovine serum (FBS) and 1% penicillin–streptomycin and incubated at 37 °C under a 5% CO₂ atmosphere. To culture CD8⁺ T cells, the cells from spleen and lymph nodes of 6 week old C57BL/6 mice were purified using CD8-conjugated magnetic beads (Miltenyi Biotec, Germany) and cultured in Roswell Park Memorial Institute (RPMI) medium containing 10% FBS and 1% penicillin–streptomycin.

Cytotoxicity. Viabilities of the cells after treatments with BP-cF and BP-DcF@sPL in the absence and presence of NIR irradiation, including individual D, were determined by MTS assay. Briefly, the cells were seeded in 96-well plates at 1×10^4 cells per well and incubated for 24 h. The cells were then treated with the configurations at different concentrations (1.25–20.00 μ g/mL) and cultured for 24 h. For the NIR cases, the irradiation (808 nm, 1.5 W/cm², 5 min) was performed after 6 h of incubation. After the incubation was completed, MTS solution was added into each well, and the absorbance was measured at a wavelength of 493 nm using a microplate reader (Multiskan EX; Thermo Scientific, USA) after a further 4 h of incubation.

Cellular Uptake. MC-38, HCT116, or HT29 cells were seeded on a 12-well plate at 1×10^5 cells per well and incubated for 24 h. The cells were then treated with BP-DcF@sPL (with and without F pretreatment at 5 μ g/mL D and 50 nM s) at 37 °C for 6 h. After incubation, the cells were harvested and washed with PBS before analysis using a FACSCalibur flow cytometer (BD Biosciences, USA). Localizations of BP-DcF@sPL (with and without F pretreatment) in the cells were observed using CLSM (Leica Microsystems, Germany). Briefly, cells (2×10^5) were attached on a round glass coverslip and then treated with the configurations in serum-free medium for 6 h. After being washed with cold PBS, the cells were stained with Lyso-tracker green for 20 min and then fixed with 4% paraformaldehyde. The prepared specimens were visualized using CLSM after staining with 4',6'-diamidino-2-phenylindole (DAPI) for 10 min. For the endosomal escape study, cells were seeded and treated with the same formulation mentioned above in the presence of NIR (808 nm, 1.5 W/cm², 5 min). The fluorescein amidite-labeled s and Lyso-tracker red were used to visualize combinatorial cellular maps.

In Vitro PL Expression and sPL Silencing. To confirm PL expression, MC-38, HCT116, or HT29 cells were seeded on a 6-well plate at 1×10^5 cells per well with 2 mL of culture medium containing IFN- γ (20 ng/mL). After 48 h of incubation, the cells were lysed, and proteins were then collected for Western blotting. PL expression levels upon IFN- γ stimulation were detected at incubation times at 0, 12, 24, and 48 h. To investigate the sPL-silencing effect, cells were stimulated with 20 ng/mL IFN- γ and treated with BP-DcF@sPL at different PL concentrations (10–100 nM at 5.0 μ g/mL D and 50 nM s). The scramble s group was the negative control used for comparison purposes. After 48 h of incubation, the cells were lysed, and proteins were then collected for Western blotting. PL silencing in cells incubated with sPL, BP-DcF, BP-DcF+sPL (not encapsulating sPL), BP-DcF@sPL, and Dharmafect@sPL was further assessed by Western blotting and flow cytometry [by staining the cell surfaces with phycoerythrin (PE) anti-mouse PL antibody]. In Western blotting, the protein samples were harvested and quantified by the bicinchoninic acid assay after centrifugation (12 000g) of cell lysates at 4 °C for 20 min. The proteins were then separated on 10% sodium dodecyl sulfate polyacrylamide gel electrophoresis and transferred to nitrocellulose membranes. After being blocked with 5% skim milk at 37 °C for 1 h, the membranes were rinsed three times with Tris-buffered saline with 0.1% Tween 20 (TBST). The membranes were subsequently incubated overnight with PL or glyceraldehyde-3-phosphate dehydrogenase (GAPDH) primary antibody. The membranes were washed with TBST and incubated with secondary immunoglobulin G-horseradish peroxidase antibody for 1 h at room temperature, before contrast images were taken from the chemiluminescence. Folate receptor expression levels in the cell lines were further confirmed through Western blotting according to the identical method mentioned above for sample preparation.

In Vitro ROS Generation and Apoptosis. MC-38 cells were seeded on a 12-well plate at 1×10^5 cells per well and incubated overnight. The cells were then treated with the configurations (at 5.0 μ g/mL D and 50 nM s). For NIR cases, the irradiation (808 nm, 1.5 W/cm², 5 min) was performed after 6 h of incubation, and the cells were further incubated for 24 h. The cells were collected and stained with 20 μ M DCFDA for 30 min before flow cytometry to detect ROS generation. Subsequent apoptosis from the ROS generation was analyzed *via* live/dead assay and Annexin V/PI staining. Briefly, identically treated MC-38 cells for ROS detection were stained with acridine orange (6.7 μ M) and PI (750 μ M) in RPMI medium. After being washed with PBS three times, the specimens were observed using a fluorescence microscope (Eclipse Ti; Nikon, USA). To quantify the apoptotic cell fractions, the treated cells were analyzed by FACSCalibur flow cytometry (BD Biosciences, USA) after collection and staining using an Annexin V/PI kit (BD Biosciences, USA).

Competitive Uptake in the Coculture System. Dendritic cells (bone-derived) were harvested from femurs of C57BL/6 mice under stimulation with 10 ng/mL of interleukin 4 and 20 ng/mL of granulocyte–macrophage colony-stimulating factor for 7 days. To isolate CD8⁺ T cells, single-cell suspensions were isolated from spleen and lymph nodes of 6 week old C57BL/6 mice. CD4⁺ T cells were purified with CD4MicroBeads, whereas purified CD8⁺ T cells were obtained using MidiMACS sorting device (Miltenyi Biotec, Germany) by adding CD8MicroBeads. Competitive uptake of BP-DcF@sPL between MC-38 and CD8⁺ T, MC-38 and dendritic, or MC-38 and RAW264.7 cells in the coculture system was investigated using Transwell plates. MC-38 (1×10^5 cells per well) and CD8⁺ T (or dendritic, or RAW264.7; 1×10^5 cells per well) cells were seeded on Transwells (0.4 μ m pore size); thus, each well of the plate contained both MC-38 and CD8⁺ T, MC-38 and dendritic, or MC-38 and RAW264.7 cells. After 24 h of incubation, BP-Dc@s and BP-DcF@s (at 2.5 μ g/mL D and 50 nM s) were added to the plate. After a further 6 h of incubation, cells in the Transwells were collected and washed with PBS, and the uptake was measured by a FACSCalibur flow cytometer (BD Biosciences, USA).

Hemolysis. Whole blood withdrawn from C57BL/6 mice was centrifuged at 500g and washed three times with PBS to remove plasma. A total of 0.5 mL of 4% erythrocytes (v/v) was then mixed

with 0.5 mL of distilled water, PBS, and BP-DcF@sPL (or BP; at concentrations of 25, 50, 100, and 200 μ g/mL). After 8 h of incubation at 37 °C, the erythrocytes were spun down, and the absorbance of the suspension was measured using a UV–vis spectrophotometer (U-2800; PerkinElmer, USA) at wavelength of 540 nm. The percentage hemolysis was estimated as follows: hemolysis (%) = $(A/A_0) \times 100\%$, where A and A₀ represent the absorbances of BP-DcF@sPL (or BP) and erythrocyte (in distilled water)-containing suspensions, respectively.

In Vivo Biodistribution. To measure biodistributions, MC-38 cells (1×10^6 cells per mice) were injected into the flank of C57BL/6 mice to establish the *in vivo* tumor models. BP-Dc@Cy5.5-s with or without F (at 5.0 mg/kg D and 30 μ g of Cy5.5-s per mouse) was intravenously injected into the mice (N = 6) when the tumor size reached 500 mm³. At 0, 12, and 24 h postinjection, mice were anesthetized, and the fluorescence was acquired using an *in vivo* imaging system (FOBI; NeoScience, Republic of Korea). Twenty-four hours after injection, the mice were killed, and *ex vivo* fluorescence distributions in heart, liver, spleen, lung, kidney, and tumor were also analyzed. All animal experiments were performed in compliance with the guidelines and regulations of the Institutional Animal Ethical Committee, Yeungnam University, Republic of Korea.

The distribution of D from intravenous injection of BP-DcF@sPL (at 5.0 mg/kg D and 30 μ g of sPL per mouse) and free D was measured in MC-38 tumor-bearing mice having ~ 500 mm³ tumors. After 24 h, the mice were sacrificed and heart, liver, spleen, lung, kidney, and tumors were harvested and weighed. Following homogenization in the presence of lysis buffer (comprising 40 mM Tris acetate, 1% Triton-100, 10 mM dithiothreitol, 10 mM ethylenediaminetetraacetic acid, and 1% sodium dodecyl sulfate), D was extracted using HCl/isopropyl alcohol and determined using HPLC (CM5000, Hitachi, Japan). The distribution of D in the organs and tumors was represented as injected dose per unit tissue mass (% ID/g).

In Vivo Photothermal Activity. To measure temperature elevations near tumor regions, MC-38 tumor-bearing mice having ~ 500 mm³ tumors were intravenously injected with BP-Dc@Cy5.5-s with or without F (at 5.0 mg/kg D and 30 μ g of Cy5.5-s per mouse). Eight hours after injection, mice were exposed to an NIR laser (808 nm, 1.5 W/cm²) for 5 min. The temperature contours were recorded using a digital thermal camera (Therm-App TH, Israel) during the exposure.

In Vivo Combination Antitumor Study. To assess antitumor effects, MC-38 tumor-bearing C57BL/6 mice were randomly divided into eight groups (N = 6) and intravenously injected with BP-DcF (at D concentration of 5.0 mg/kg) and BP-DcF@sPL (D concentration of 5.0 mg/kg and 30 μ g of s per mouse) in the absence and presence of NIR irradiation, including individual PBS, NIR, and D with BP-DcF+aPL (in the presence of NIR) for comparison purposes. Eight hours after injection, NIR cases were irradiated with an NIR laser (808 nm, 1.5 W/cm²) for 5 min. The treatments were continued every 2 days until the end of the antitumor study. During this period, tumor volumes and body weights were monitored daily, and the tumor volume was calculated as follows: volume = $[\text{length} \times (\text{width})^2]/2$. To specifically examine the phototherapeutic effect, mice were killed on day 16, and tumor masses were collected. A single-cell suspension was acquired after mechanical dissociation and passage through a 100 μ m strainer (Falcon; BD Biosciences, USA). The cell suspension was then stained with DCFDA (20 μ M) for 30 min, and quantitative ROS generation in the tumor was measured by a FACSCalibur flow cytometer (BD Biosciences, USA).

In the case of antitumor immunity, tumor masses were separated from the C57BL/6 mice on day 16 and mechanically dissociated into a single-cell suspension. The dissociated cells were then stained with fluorescein isothiocyanate (FITC) anti-mouse CD11c⁺, PE anti-mouse CD86⁺, adenomatous polyposis coli (APC) anti-mouse CD69⁺, and Percp-Cy5.5 anti-mouse CD8⁺. The levels of mature DCs and CD8⁺ T cells were subsequently analyzed by a FACSVerse flow cytometer (BD Biosciences, USA). The homogenate was also collected from the tumor masses; thus, the levels of tumor necrosis

factor α (TNF- α) secreted in association with the treatments were detected using an enzyme-linked immunosorbent assay (ELISA) kit (Invitrogen, USA). To confirm the *in vivo* sPL-silencing effect, the isolated cell suspension was stained with PE anti-mouse PL, and the signals were measured by the flow cytometer. To detect the intracellular IFN- γ secreted by CD8 $^{+}$ T cells, the isolated cells were stimulated with 50 ng/mL phorbol 12-myristate 13-acetate, 500 ng/mL ionomycin (eBioscience, USA), and 1 μ L/mL GolgiStop (BD Biosciences, USA) for 4 h. The cells were then stained with FITC anti-mouse CD3 $^{+}$, APC anti-mouse IFN- γ , and Percp-Cy5.5 anti-mouse CD8 $^{+}$, and the signals were captured by flow cytometry. The apoptotic tumor cells after the treatments were also analyzed by flow cytometry after staining with the Annexin V/PI kit. Also, the combined antitumor effects were assessed in HCT116 tumor-bearing mice ($N = 6$) after treatments with BP-DcF (at D concentration of 5.0 mg/kg) and BP-DcF@sPL (at D concentration of 5.0 mg/kg and 30 μ g of s per mouse) in the absence and presence of NIR irradiation (808 nm, 1.5 W/cm 2 , 5 min, 6 h postinjection), including individual PBS, NIR, and D for comparison purposes (*i.e.*, seven groups).

To assess the contribution of immunotherapy into combination tumor therapy, the depletion of CD4 $^{+}$, CD8 $^{+}$, or CD4 $^{+}$ –CD8 $^{+}$ T cells in the immunocompetent model was investigated from intraperitoneal injection of anti-CD4 (GK1.5, BioXcell, USA), anti-CD8 (2.43, BioXcell, USA), or mouse IgG (SouthernBiotech, USA). When the tumor volume reached ~ 100 mm 3 , mice were intravenously administered with BP-DcF@sPL (at D concentration of 5.0 mg/kg and 30 μ g of s per mouse) or PBS and exposed to NIR irradiation (808 nm, 1.5 W/cm 2 , 5 min, 8 h postinjection).

Statistical Analysis. All of the results are presented as mean \pm standard deviation. Student's *t*-test (for a pair of groups) and one-way analysis of variance (for more than two groups) were employed to analyze the statistical significance of the differences. The significance level was set at $*p < 0.05$.

ASSOCIATED CONTENT

Supporting Information

The Supporting Information is available free of charge on the ACS Publications website at DOI: [10.1021/acsnano.8b04658](https://doi.org/10.1021/acsnano.8b04658).

Detailed scheme for BP nanorization, UV–vis and Raman spectra of BP; DLS and UV–vis results of cF or D incorporated BP; loading capacities of BP with D, DcF, and DcF@sPL; FTIR and XRD profiles of D, cF, BP, BP-cF, and BP-DcF@sPL; EDS profile; D loading stability; folate receptor expression; s endosomal escape; PL expression upon stimulation; cellular uptake of BP-Dc@s and BP-DcF@s into MC-38 and CD8 $^{+}$ T (or dendritic, or RAW264.7) cells; *in vivo* D distribution; variations of tumor mass, histomorphometrical analyses, and antitumor effects for the treatments; and cell depletion-based *in vivo* antitumor study (PDF)

AUTHOR INFORMATION

Corresponding Authors

*E-mail: postjb@yu.ac.kr (J.H.B.).

*E-mail: csyong@yu.ac.kr (C.S.Y.).

*E-mail: jongohkim@yu.ac.kr (J.O.K.).

ORCID

Jeong Hoon Byeon: 0000-0003-0903-7128

Jong Oh Kim: 0000-0002-4929-851X

Notes

The authors declare no competing financial interest.

ACKNOWLEDGMENTS

This work was supported by the NRF of Korea Grant funded by the Korean Government (NRF-2018R1A2A2A05021143).

This research was also supported by the Medical Research Center Program (2015R1A5A2009124) through the NRF funded by MSIP.

REFERENCES

- (1) Jiao, M.; Zhang, P.; Meng, J.; Li, Y.; Liu, C.; Luo, X.; Gao, M. Recent Advancements in Biocompatible Inorganic Nanoparticles towards Biomedical Applications. *Biomater. Sci.* **2018**, *6*, 726–745.
- (2) Soenen, S. J.; Parak, W. J.; Rejman, J.; Manshian, B. (Intra)Cellular Stability of Inorganic Nanoparticles: Effects on Cytotoxicity, Particle Functionality, and Biomedical Applications. *Chem. Rev.* **2015**, *115*, 2109–2135.
- (3) Paramasivam, G.; Kayambu, N.; Rabel, A. M.; Sundramoorthy, A. K.; Sundaramurthy, A. Anisotropic Noble Metal Nanoparticles: Synthesis, Surface Functionalization and Applications in Biosensing, Bioimaging, Drug Delivery and Theranostics. *Acta Biomater.* **2017**, *49*, 45–65.
- (4) Chen, Y.; Wang, L.; Shi, J. Two-Dimensional Non-Carbonaceous Materials-Enabled Efficient Photothermal Cancer Therapy. *Nano Today* **2016**, *11*, 292–308.
- (5) Yi, Y.; Yu, X.-F.; Zhou, W.; Wang, J.; Chu, P. K. Two-Dimensional Black Phosphorus: Synthesis, Modification, Properties, and Applications. *Mater. Sci. Eng., R* **2017**, *120*, 1–33.
- (6) Qiu, M.; Wang, D.; Liang, W.; Liu, L.; Zhang, Y.; Chen, X.; Sang, D. K.; Xing, C.; Li, Z.; Dong, B.; Xing, F.; Fan, D.; Bao, S.; Zhang, H.; Cao, Y. Novel Concept of the Smart NIR-Light-Controlled Drug Release of Black Phosphorus Nanostructure for Cancer Therapy. *Proc. Natl. Acad. Sci. U. S. A.* **2018**, *115*, 501–506.
- (7) Xing, C.; Chen, S.; Qiu, M.; Liang, X.; Liu, Q.; Zou, Q.; Li, Z.; Xie, Z.; Wang, D.; Dong, B.; Liu, L.; Fan, D.; Zhang, H. Conceptually Novel Black Phosphorus/Cellulose Hydrogels as Promising Photothermal Agents for Effective Cancer Therapy. *Adv. Healthcare Mater.* **2018**, *7*, 1701510.
- (8) Zhao, Y.; Tong, L.; Li, Z.; Yang, N.; Fu, H.; Wu, L.; Cui, H.; Zhou, W.; Wang, J.; Wang, H.; Chu, P. K.; Yu, X.-F. Stable and Multifunctional Dye-Modified Black Phosphorus Nanosheets for Near-Infrared Imaging-Guided Photothermal Therapy. *Chem. Mater.* **2017**, *29*, 7131–7139.
- (9) Li, Y.; Liu, Z.; Hou, Y.; Yang, G.; Fei, X.; Zhao, H.; Guo, Y.; Su, C.; Wang, Z.; Zhong, H.; Zhuang, Z.; Guo, Z. Multifunctional Nanoplatfrom Based on Black Phosphorus Quantum Dots for Bioimaging and Photodynamic/Photothermal Synergistic Cancer Therapy. *ACS Appl. Mater. Interfaces* **2017**, *9*, 25098–25106.
- (10) Poudel, B. K.; Hwang, J.; Ku, S. K.; Kim, J. O.; Byeon, J. H. A Batch-by-Batch Free Route for the Continuous Production of Black Phosphorus Nanosheets for Targeted Combination Cancer Therapy. *NPG Asia Mater.* **2018**, DOI: [10.1038/s41427-018-0068-8](https://doi.org/10.1038/s41427-018-0068-8).
- (11) Tao, W.; Zhu, X.; Yu, X.; Zeng, X.; Xiao, Q.; Zhang, X.; Ji, X.; Wang, X.; Shi, J.; Zhang, H.; Mei, L. Black Phosphorus Nanosheets as a Robust Delivery Platform for Cancer Theranostics. *Adv. Mater.* **2017**, *29*, 1603276.
- (12) Chen, W.; Qin, M.; Chen, X.; Wang, Q.; Zhang, Z.; Sun, X. Combining Photothermal and Immunotherapy against Melanoma by Polydopamine-Coated Al $_2$ O $_3$ Nanoparticles. *Theranostics* **2018**, *8*, 2229–2241.
- (13) Mu, X.; Wang, J.-Y.; Bai, X.; Xu, F.; Liu, H.; Yang, J.; Jing, Y.; Liu, L.; Xue, X.; Dai, H.; Liu, Q.; Sun, Y.-M.; Liu, C.; Zhang, X.-D. Black Phosphorus Quantum Dot Induced Oxidative Stress and Toxicity in Living Cells and Mice. *ACS Appl. Mater. Interfaces* **2017**, *9*, 20399–20409.
- (14) Mao, C.; Xiang, Y.; Liu, X.; Cui, Z.; Yang, X.; Li, Z.; Zhu, S.; Zheng, Y.; Yeung, K. W. W.; Wu, S. Repeatable Photodynamic Therapy with Triggered Signaling Pathways of Fibroblast Cell Proliferation and Differentiation to Promote Bacteria-Accompanied Wound Healing. *ACS Nano* **2018**, *12*, 1747–1759.
- (15) Nam, J.; Son, S.; Ochyl, L. J.; Kuai, R.; Schwendeman, A.; Moon, J. J. Chemo-Photothermal Therapy Combination Elicits Anti-

Tumor Immunity against Advanced Metastatic Cancer. *Nat. Commun.* **2018**, *9*, 1074.

(16) Tao, Y.; Ju, E.; Liu, Z.; Dong, K.; Ren, J.; Qu, X. Engineered, Self-Assembled Near-Infrared Photothermal Agents for Combined Tumor Immunotherapy and Chemo-Photothermal Therapy. *Biomaterials* **2014**, *35*, 6646–6656.

(17) Chen, Q.; Xu, L.; Liang, C.; Wang, C.; Peng, R.; Liu, Z. Photothermal Therapy with Immune-Adjuvant Nanoparticles together with Checkpoint Blockade for Effective Cancer Immunotherapy. *Nat. Commun.* **2016**, *7*, 13193.

(18) Luo, L.; Shu, R.; Wu, A. Nanomaterial-Based Cancer Immunotherapy. *J. Mater. Chem. B* **2017**, *5*, 5517–5531.

(19) Pan, J.; Wang, Y.; Zhang, C.; Wang, X.; Wang, H.; Wang, J.; Yuan, Y.; Wang, X.; Zhang, X.; Yu, C.; Sun, S.-K.; Yan, X.-P. Antigen-Directed Fabrication of a Multifunctional Nanovaccine with Ultrahigh Antigen Loading Efficiency for Tumor Photothermal-Immunotherapy. *Adv. Mater.* **2018**, *30*, 1704408.

(20) Xu, J.; Xu, L.; Wang, C.; Yang, R.; Zhuang, Q.; Han, X.; Dong, Z.; Zhu, W.; Peng, R.; Liu, Z. Near-Infrared-Triggered Photodynamic Therapy with Multitasking Upconversion Nanoparticles in Combination with Checkpoint Blockade for Immunotherapy of Colorectal Cancer. *ACS Nano* **2017**, *11*, 4463–4474.

(21) Callahan, M. K.; Postow, M. A.; Wolchok, J. D. Targeting T Cell Co-Receptors for Cancer Therapy. *Immunity* **2016**, *44*, 1069–1078.

(22) Juneja, V. R.; McGuire, K. A.; Manguso, R. T.; LaFleur, M. W.; Collins, N.; Haining, W. N.; Freeman, G. J.; Sharpe, A. H. PD-L1 on Tumor Cells is Sufficient for Immune Evasion in Immunogenic Tumors and Inhibits CD8 T Cell Cytotoxicity. *J. Exp. Med.* **2017**, *214*, 895–904.

(23) Moy, A. J.; Tunnell, J. W. Combinatorial Immunotherapy and Nanoparticle Mediated Hyperthermia. *Adv. Drug Delivery Rev.* **2017**, *114*, 175–183.

(24) Rubio-Pereda, P.; Coccoletti, G. H. Density Functional Theory Calculations of Biomolecules Adsorption on Phosphorene for Biomedical Applications. *Appl. Surf. Sci.* **2018**, *427*, 1227–1234.

(25) Wang, D.; Wang, T.; Liu, J.; Yu, H.; Jiao, S.; Feng, B.; Zhou, F.; Fu, Y.; Yin, Q.; Zhang, P.; Zhang, Z.; Zhou, Z.; Li, Y. Acid-Activatable Versatile Micelleplexes for PD-L1 Blockade-Enhanced Cancer Photodynamic Immunotherapy. *Nano Lett.* **2016**, *16*, 5503–5513.

(26) Kwak, G.; Kim, D.; Nam, G.-h.; Wang, S. Y.; Kim, I.-S.; Kim, S. H.; Kwon, I.-C.; Yeo, Y. Programmed Cell Death Protein Ligand-1 Silencing with Polyethylenimine–Dermatan Sulfate Complex for Dual Inhibition of Melanoma Growth. *ACS Nano* **2017**, *11*, 10135–10146.

(27) Whitehead, K. A.; Langer, R.; Anderson, D. G. Knocking Down Barriers: Advances in siRNA Delivery. *Nat. Rev. Drug Discovery* **2009**, *8*, 129–148.

(28) Yin, F.; Hu, K.; Chen, S.; Wang, D.; Zhang, J.; Xie, M.; Yang, D.; Qiu, M.; Zhang, H.; Li, Z.-g. Black Phosphorus Quantum Dot Based Novel siRNA Delivery Systems in Human Pluripotent Teratoma PA-1 Cells. *J. Mater. Chem. B* **2017**, *5*, 5433–5440.

(29) Chakraborty, A.; Boer, J. C.; Selomulya, C.; Plebanski, M. Amino Acid Functionalized Inorganic Nanoparticles as Cutting-Edge Therapeutic and Diagnostic Agents. *Bioconjugate Chem.* **2018**, *29*, 657–671.

(30) Shao, J.; Xie, H.; Huang, H.; Li, Z.; Sun, Z.; Xu, Y.; Xiao, Q.; Yu, X.-F.; Zhao, Y.; Zhang, H.; Wang, H.; Chu, P. K. Biodegradable Black Phosphorus-Based Nanospheres for *In Vivo* Photothermal Cancer Therapy. *Nat. Commun.* **2016**, *7*, 12967.

(31) Zhang, X.; Zhang, Z.; Zhang, S.; Li, D.; Ma, W.; Ma, C.; Wu, F.; Zhao, Q.; Yan, Q.; Xing, B. Size Effect on the Cytotoxicity of Layered Black Phosphorus and Underlying Mechanisms. *Small* **2017**, *13*, 1701210.

(32) Qian, X.; Gu, Z.; Chen, Y. Two-Dimensional Black Phosphorus Nanosheets for Theranostic Nanomedicine. *Mater. Horiz.* **2017**, *4*, 800–816.

(33) Yang, X.; Liu, G.; Shi, Y.; Huang, W.; Shao, J.; Dong, X. Nano-Black Phosphorus for Combined Cancer Phototherapy: Recent Advances and Prospects. *Nanotechnology* **2018**, *29*, 222001.

(34) Sun, C.; Wen, L.; Zeng, J.; Wang, Y.; Sun, Q.; Deng, L.; Zhao, C.; Li, Z. One-Pot Solventless Preparation of PEGylated Black Phosphorus Nanoparticles for Photoacoustic Imaging and Photothermal Therapy of Cancer. *Biomaterials* **2016**, *91*, 81–89.

(35) Lee, J. S.; Weon, B. M.; Park, S. J.; Je, J. H.; Fezzaa, K.; Lee, W.-K. Size Limits the Formation of Liquid Jets During Bubble Bursting. *Nat. Commun.* **2011**, *2*, 367.

(36) Fröhlich, E. The Role of Surface Charge in Cellular Uptake and Cytotoxicity of Medical Nanoparticles. *Int. J. Nanomed.* **2012**, *7*, 5577–5591.

(37) Zhang, J.; Yu, X.; Han, W.; Lv, B.; Li, X.; Xiao, S.; Gao, Y.; He, J. Broadband Spatial Self-Phase Modulation of Black Phosphorus. *Opt. Lett.* **2016**, *41*, 1704–1707.

(38) Korolkov, V. V.; Timokhin, I. G.; Haubrichs, R.; Smith, E. F.; Yang, L.; Yang, S.; Champness, N. R.; Schröder, M.; Beton, P. H. Supramolecular Networks Stabilise and Functionalise Black Phosphorus. *Nat. Commun.* **2017**, *8*, 1385.

(39) Petryszak, R.; Keays, M.; Tang, Y. A.; Fonseca, N. A.; Barrera, E.; Burdett, T.; Füllgrabe, A.; Fuentes, A. M.-P.; Jupp, S.; Koskinen, S.; Mannion, O.; Huerta, L.; Megy, K.; Snow, C.; Williams, E.; Barzine, M.; Hastings, E.; Weisser, H.; Wright, J.; Jaiswal, P.; et al. Expression Atlas Update—An Integrated Database of Gene and Protein Expression in Humans, Animals and Plants. *Nucleic Acids Res.* **2016**, *44*, D746–D752.

(40) Kobayashi, T.; Ishida, T.; Okada, Y.; Ise, S.; Harashima, H.; Kiwada, H. Effect of Transferrin Receptor-Targeted Liposomal Doxorubicin in P-Glycoprotein-Mediated Drug Resistant Tumor Cells. *Int. J. Pharm.* **2007**, *329*, 94–102.

(41) Mandai, M.; Hamanishi, J.; Abiko, K.; Matsumura, N.; Baba, T.; Konishi, I. Dual Faces of IFN γ in Cancer Progression: A Role of PD-L1 Induction in the Determination of Pro- and Antitumor Immunity. *Clin. Cancer Res.* **2016**, *22*, 2329–2334.

(42) Salgado, R.; Denkert, C.; Demaria, S.; Sirtaine, N.; Klauschen, F.; Pruneri, G.; Wienert, S.; Van den Eynden, G.; Baehner, F. L.; Penault-Llorca, F.; Perez, E. A.; Thompson, E. A.; Symmans, W. F.; Richardson, A. L.; Brock, J.; Criscitiello, C.; Bailey, H.; Ignatiadis, M.; Floris, G.; Sparano, J.; et al. The Evaluation of Tumor-Infiltrating Lymphocytes (TILs) in Breast Cancer: Recommendations by an International TILs Working Group 2014. *Ann. Oncol.* **2015**, *26*, 259–271.

(43) Castano, A. P.; Mroz, P.; Hamblin, M. R. Photodynamic Therapy and Anti-Tumour Immunity. *Nat. Rev. Cancer* **2006**, *6*, 535–545.

(44) Reginato, E.; Wolf, P.; Hamblin, M. R. Immune Response After Photodynamic Therapy Increases Anti-Cancer and Anti-Bacterial Effects. *World J. Immunol.* **2014**, *4*, 1–11.

(45) Peng, W.; Liu, C.; Xu, C.; Lou, Y.; Chen, J.; Yang, Y.; Yagita, H.; Overwijk, W. W.; Lizée, G.; Radvanyi, L.; Hwu, P. PD-1 Blockade Enhances T-Cell Migration to Tumors by Elevating IFN- γ Inducible Chemokines. *Cancer Res.* **2012**, *72*, 5209–5218.

(46) Donia, M.; Hansen, M.; Sendrup, S. L.; Iversen, T. Z.; Ellebæk, E.; Andersen, M. H.; Straten, P. t.; Svane, I. M. Methods to Improve Adoptive T-Cell Therapy for Melanoma: IFN- γ Enhances Anticancer Responses of Cell Products for Infusion. *J. Invest. Dermatol.* **2013**, *133*, 545–552.

(47) Nilges, T.; Kersting, M.; Pfeifer, T. A Fast Low-Pressure Transport Route to Large Black Phosphorus Single Crystals. *J. Solid State Chem.* **2008**, *181*, 1707–1711.